

Magnetoelectric Control of Helical Light Emission in a Moiré Chern Magnet

Eric Anderson^{1,*}, Heonjoon Park,¹ Kaijie Yang,² Jiaqi Cai¹, Takashi Taniguchi³,
Kenji Watanabe⁴, Liang Fu,⁵ Ting Cao,² Di Xiao^{2,1,†} and Xiaodong Xu^{1,2,‡}

¹Department of Physics, *University of Washington*, Seattle, Washington 98195, USA

²Department of Materials Science and Engineering,
University of Washington, Seattle, Washington 98195, USA

³Research Center for Materials Nanoarchitectonics, *National Institute for Materials Science*,
1-1 Namiki, Tsukuba 305-0044, Japan

⁴Research Center for Electronic and Optical Materials, *National Institute for Materials Science*,
1-1 Namiki, Tsukuba 305-0044, Japan

⁵Department of Physics, *Massachusetts Institute of Technology*, Cambridge, Massachusetts 02139, USA

 (Received 27 February 2025; revised 23 June 2025; accepted 22 July 2025; published 27 August 2025)

Magnetoelectric effects and their coupling to light helicity are important for both fundamental science and applications in sensing, communication, and data storage. Traditional approaches require complex device architectures, involving separate spin-injection, ferromagnetic, and optically active layers. Recently, the emergence of 2D semiconductor moiré superlattices with flat Chern bands and strong light-matter interactions has established a simple yet powerful platform for exploring the coupling between photon, electron, and spin degrees of freedom. Here, we report efficient current control of spontaneous ferromagnetism and associated helicity of light emission in moiré MoTe₂ bilayer—a system which hosts a rich variety of topological phases, including newly discovered zero-field fractional Chern insulators. We show that the current control is effective over a wide range of doping of the first moiré Chern band, implying the uniformity of the Berry curvature distribution over the flat band. By setting the system into the anomalous Hall metal phase, a current as small as 10 nA is sufficient to switch the magnetic order, a substantial improvement over both conventional spin-torque architectures and other moiré systems. The realized current control of ferromagnetism leads to continuous tuning of trion photoluminescence helicity from left to right circular via spin-valley Hall torque at zero magnetic field. Our results pave the way for topological optospintronics based on semiconductors with synthetic flat Chern bands.

DOI: [10.1103/ds5p-763x](https://doi.org/10.1103/ds5p-763x)

Subject Areas: Optoelectronics, Spintronics,
Strongly Correlated Materials

I. INTRODUCTION

Moiré superlattice engineering has been proven to be an effective approach for creating new phases of matter with exotic physical properties [1–3]. A striking example is the recent discovery of the fractional quantum anomalous Hall (FQAH) effect in twisted MoTe₂ bilayer [4–10] (tMoTe₂) and rhombohedral-stacked multilayer graphene, [11] realizing long-sought zero-field fractional Chern

insulators. [12–18] Besides hosting the FQAH effect, the semiconducting transition-metal-dichalcogenide (TMD) tMoTe₂ is a direct band-gap semiconductor, with spin-valley locking and a strong excitonic response [19–21]. These properties have enabled optical probing of the Chern insulator [4] and putative composite Fermi liquid [10] states via measurement of the intensity and helicity of trion photoluminescence. In addition, both electric field and doping have been demonstrated to be effective controls of the spontaneous ferromagnetic order in tMoTe₂ [21], enabling powerful magnetoelectric manipulation.

The physical properties of tMoTe₂ mentioned above offer a new means to manipulate intrinsic magnetism—and thus light-emission helicity, which is tightly linked with spin-valley polarization—via electric current. Current control of light-emission helicity is highly sought after, as it involves coupling the relevant degrees of freedom in electronics, spintronics, and photonics. This functionality has recently been achieved in complex multilayer architectures [22]. For these devices, charge current in a

*Present address: Université Paris-Saclay, CNRS, Centre de Nanosciences et de Nanotechnologies (C2N), Palaiseau 91120, France.

†Contact author: dixiao@uw.edu

‡Contact author: xuxd@uw.edu

Published by the American Physical Society under the terms of the [Creative Commons Attribution 4.0 International](https://creativecommons.org/licenses/by/4.0/) license. Further distribution of this work must maintain attribution to the author(s) and the published article's title, journal citation, and DOI.

layer with strong spin-orbit coupling generates a spin current, and the resulting spin-orbit torque enables magnetization switching in an adjacent ferromagnetic layer. This further allows for injection of spin-polarized carriers into a separate optically active layer. However, the degree of circular polarization of emitted light is limited, largely due to the spatial separation between the spin current generating and the optically active layers.

Here, we realized spin-valley Hall-torque-driven magnetization switching and current-controlled helical light emission in tMoTe₂. Remarkably, the degree of circular polarization can be continuously tuned, and reaches nearly perfect circular polarization at a small applied current. This is achieved via three unusual properties of the system. First, the necessary ingredients—spin-torque control of magnetic order and spin-polarization-dependent helical emission—occur within a single direct band-gap semiconductor system, overcoming the challenge of multilayer structures. Second, flat Chern bands with nearly uniform Berry curvature and spin-valley locking effects enable efficient spin-valley polarization control over a large doping range.

Third, tMoTe₂ hosts rich and electrically tunable quantum phases. Tuning the system into an anomalous Hall metal phase [23], i.e., a metallic phase with anomalous Hall effect, increases the efficiency of current control. Below, we present results from two tMoTe₂ devices, D(3.7°) and D(3.9°), with twist angles of 3.7° and 3.9°. Both devices host integer and fractional QAH states, as detailed in prior reports [6,8].

II. RESULTS AND DISCUSSION

A. Anomalous Hall metal

We begin with an exploration of the anomalous Hall metal phase (AHM). Figure 1(a) shows a schematic of the dual-gated device and an atomic-force-microscopy (AFM) image of D(3.9°). The clean surface implies a high device quality. Figure 1(b) is a plot of longitudinal resistance (R_{xx}) as a function of the doping and out-of-plane electric field (or displacement field) D/ϵ_0 . Data are taken at a temperature of 100 mK in D(3.7°) and symmetrized at magnetic field $\mu_0 H = \pm 100$ mT. As identified in a prior report [6],

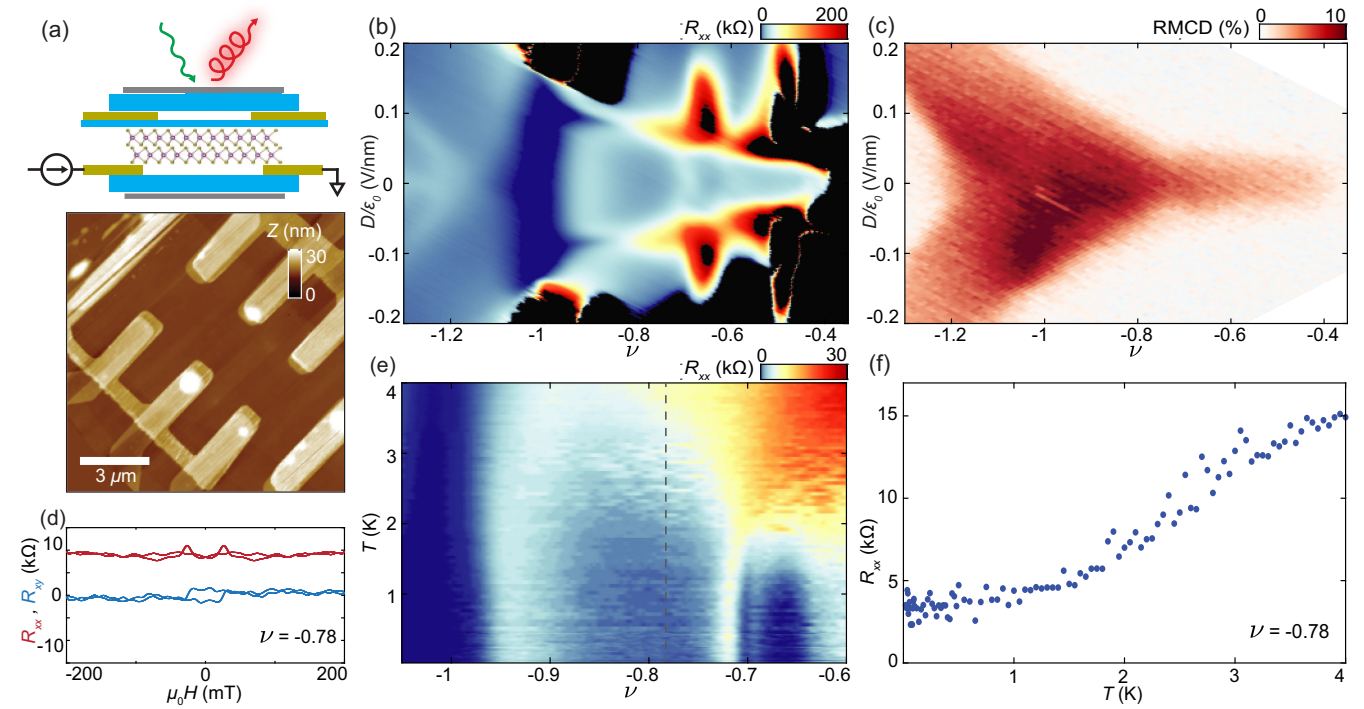


FIG. 1. Anomalous Hall metal in moiré tMoTe₂. (a) Top: schematic of the device cross section, with graphite gates in gray, BN dielectric layers in blue, and Pt contacts in yellow. Top Pt gates are used to improve contact transparency, and current is injected via the sample contacts. Optical probes can be used to reveal spontaneous spin-valley polarization with current controls. Bottom: AFM image of device D(3.9°) with contacts for current injection visible. (b) Longitudinal resistance R_{xx} vs moiré filling ν and displacement field D/ϵ_0 in D(3.7°), consistent with previous measurements. Resistance in black regions is too high to be reliably measured. R_{xx} is symmetrized at $|\mu_0 H| = 200$ mT. (c) As in (b), but measuring RMCD. Region with finite RMCD signal is ferromagnetic. Sample was measured at $\mu_0 H = 25$ mT to prevent domain flipping as gates were swept. (d) Longitudinal (R_{xx}) and Hall (R_{xy}) resistance vs magnetic field in the AHM metal regime. R_{xy} hysteresis and nonvanishing signal at 0 T are signatures of the anomalous Hall effect. (e) Temperature dependence of R_{xx} vs ν in D(3.9°). (f) Temperature dependence of R_{xx} at $\nu = -0.78$, extracted along the dotted line in (e). Increasing resistance with the temperature indicates metallic behavior.

there are QAH and FQAH phases near hole fillings $\nu = -1$ and $\nu = -2/3$, respectively, with suppressed R_{xx} . Here, ν is the filling factor denoting the number of carriers per moiré unit cell. Between $\nu = -1$ and $-2/3$, R_{xx} is also suppressed, while R_{xy} is finite but smaller than R_{xx} .

A measurement of reflective magnetic circular dichroism (RMCD) at 25 mT in the same region of phase space is shown in Fig. 1(c). All optical measurements are taken at 1.6 K unless otherwise indicated. The small applied magnetic field is to suppress spin fluctuations due to the doping sweep (see Fig. S1 in Supplemental Material [24]). As RMCD is sensitive to spin-valley polarization, the measurement reveals the ferromagnetic phase space versus ν and D/ϵ_0 . Figure 1(d) illustrates R_{xx} and R_{xy} versus $\mu_0 H$ at hole filling $\nu = -0.78$ and $D/\epsilon_0 = 0$. As shown by the RMCD measurement in Fig. 1(c), the system is in a spin-valley-polarized (ferromagnetic) regime under these conditions. R_{xy} shows clear hysteresis and is on the order of a few k Ω , while R_{xx} is nearly constant at approximately 10 k Ω , with a slight increase near the critical field $H_C \approx \pm 20$ mT where the sign of R_{xy} flips. Thus, the anomalous Hall effect is observed at this partial filling of the first moiré Chern band.

We further performed temperature-dependent measurements. Figure 1(e) shows a measurement of R_{xx} versus filling and temperature in D(3.9°). Around $\nu = -1$ and $\nu = -2/3$, R_{xx} remains nearly vanishing at low temperature and rises as the temperature is increased, when the thermal activation of the carriers over the Chern gap dominates. Between -1 and $-2/3$, R_{xx} continuously increases with the temperature. Taking a linecut at $\nu = -0.78$ (dashed line), R_{xx} increases from about 4 to 15 k Ω as the temperature increases from 100 mK to 4 K [Fig. 1(f)], suggesting a metallic phase. In addition, previous measurements of trion photoluminescence versus doping [4,10] do not show suppression of the luminescence intensity in this region of phase space, in contrast to the suppression observed at Chern insulator states. This is consistent with the compressible nature of a metallic phase. Taken together with R_{xx} being several times larger than R_{xy} , the data demonstrate the system is an AHM over this region of doping, i.e., a spontaneous ferromagnetic metal phase exhibiting an anomalous Hall signal in a partially filled Chern band.

B. Current control of spin-valley polarization

Next, we examine current control of ferromagnetism, focusing on the anomalous Hall metal phase. We employ RMCD to probe the ferromagnetic order. For instance, Fig. 2(a) shows the RMCD signal as $\mu_0 H$ is cycled at $\nu = -0.77$ and $D/\epsilon_0 = 0$, i.e., in the AHM. The clear RMCD hysteresis with finite signal at zero magnetic field is

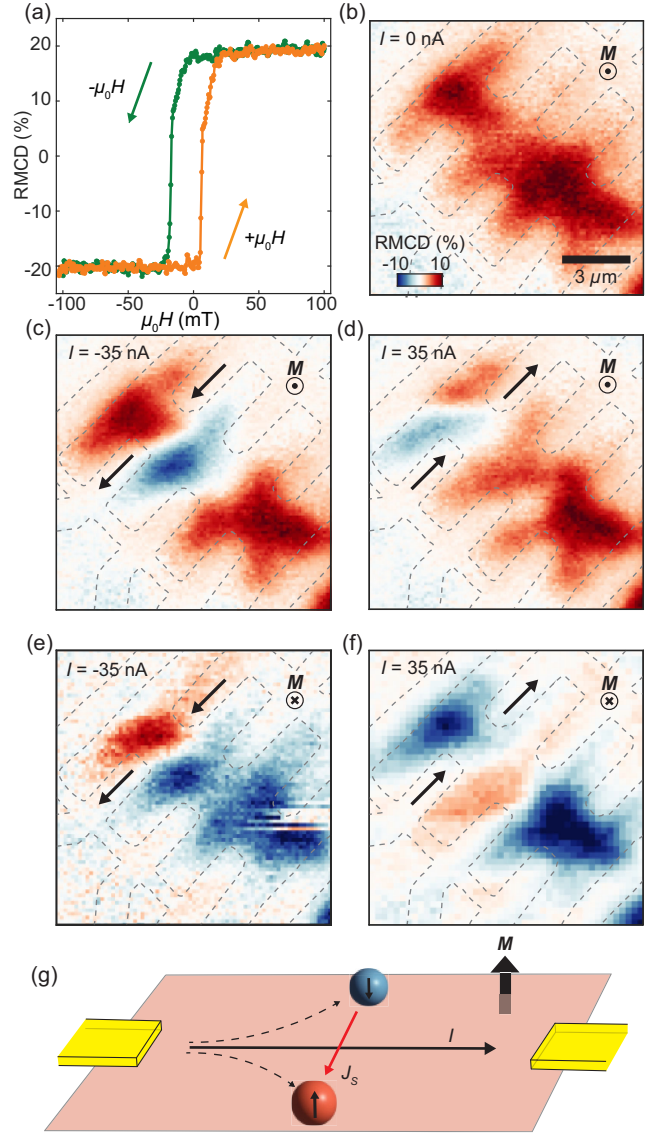


FIG. 2. Transverse spin and charge current in a ferromagnetic metal. (a) RMCD signal as a function of $\mu_0 H$ swept down and up. RMCD hysteresis demonstrates ferromagnetic order. (b) RMCD spatial map in the anomalous Hall metal regime ($\nu = -0.77$) with magnetization pointing up. Gray dashed lines indicate Pt contact area. (c) RMCD map under a current of $I = -35$ nA (indicated by the arrows) flowing between the upper-left contacts of the device. The sign change in RMCD implies the reversal of spin-valley polarization. (d) RMCD map with the current direction reversed. The sign-reversed domain appears on the opposite side of the current channel. (e) RMCD map with magnetization pointing down and $I = -35$ nA, as in (c). Despite the reversed magnetization, domain signs on either side of the current channel remain consistent with (c). (f) RMCD map with the reversed current direction and magnetization pointing down. Signs of domains on either side of the current channel match those in (d). (g) Schematic of the spin-valley Hall effect.

consistent with the observed anomalous Hall signal in Fig. 1(d). To determine the effect of the injected charge current I on the spin-valley polarization, we first took a spatial map of the RMCD signal over the entire sample at $I = 0$. Figure 2(b) shows this map for the same ν and D/ϵ_0 as in Fig. 2(a), measured at $\mu_0 H = 0$ with the magnetization initialized to point up. A finite, positive RMCD signal exists across the entire sample area, with contacts visible as regions of decreased RMCD (outlined with gray dashed lines). This is the expected behavior for a homogeneous sample tuned to the ferromagnetic (FM) phase.

In stark contrast, when an RMCD spatial map is taken under the same conditions as Fig. 2(b), but with current flowing between the two contacts on the top left, clear domains with negative RMCD signal are observed [Figs. 2(c) and 2(d)]. The current injection configuration is discussed further in Sec. IV. The opposite sign of the RMCD signal in these domains compared to the rest of the sample area demonstrates a current-driven spin-valley polarization reversal. The spatial position of the domain with reversed spin-valley polarization can be controlled by the current flow direction. For $I = -35$ nA [Fig. 2(c)], this negative domain with magnetization pointing down (blue) is to the lower right of the current channel. In contrast, for current flowing in the opposite direction [Fig. 2(d)], the negative domain is on the upper left side.

We found that the spatial pattern of current-induced polarization-reversed domains is independent of the initial magnetization orientation. The RMCD map in Fig. 2(e) is taken with the magnetization initialized to point down, as evidenced by the opposite sign of the RMCD signal on the bottom right of the map, far from the current channel. Comparing this map to Fig. 2(c) taken at $I = -35$ nA, although the initial magnetization direction is reversed, the signs of the domains on either side of the current channel are the same, i.e., positive on the upper left and negative on the lower right. Similar behavior is observed when comparing Figs. 2(d) and 2(f); for the same $I = 35$ nA current, the signs of the domains on either side of the current channel match, even though the initial magnetization directions are reversed. Varying the source-and-drain pin configuration changes the current channel and thus the locations of the domains (see Fig. S2 in Supplemental Material [24]), but the same qualitative behavior remains. Similar RMCD maps taken at selected current values (see Fig. S3 in Supplemental Material [24]) show that current-induced polarization-reversed domains are present for values of I as low as 10 nA [24].

The above measurements demonstrate that the magnetic domain pattern is determined only by the current flow direction. This results from the mechanism for current-induced magnetization flipping—spin-valley Hall torque—as shown in Fig. 2(g). The spin-valley Hall torque switching of magnetic order has been observed in $\text{MoTe}_2/\text{WSe}_2$ heterobilayer superlattices, but only near full filling of the

moiré valence band (or $\nu = -1$) [25,26]. The observation was attributed to the large Berry curvature near $\nu = -1$ [3,27,28], where the QAH effect was observed [29]. This Berry curvature generates an intrinsic spin-valley Hall effect—the source of the spin-valley-polarized current which exerts a torque on the magnetic ground state and causes the observed magnetization flipping. Our results demonstrate the same mechanism works in tMoTe_2 .

A major distinction in tMoTe_2 , however, lies in two unique aspects of the system. The first is the low current density required for magnetization switching in the anomalous Hall metal phase. At approximately 10^2 A/cm², the switching current is nearly an order of magnitude lower compared to other moiré systems [25,26]. This is most likely due to the fact that in other systems the FM phase exists only close to the insulating state, which has a relatively large spin-valley energy splitting. In contrast, in the AHM phase, the spin splitting is decreased due to carrier screening and/or partial valley polarization. The second aspect is that tMoTe_2 exhibits this current control behavior over a much larger region of phase space. Although in the above discussion we focus on the AHM, efficient current switching is observed over a broad range of fillings of the first moiré Chern band. As shown in Fig. S4 in Supplemental Material [24], the sign of RMCD changes with applied current not only near $\nu = -0.77$ but over the entire FM phase space for hole fillings below $\nu = -1$, as well as in the wings of the FM phase above $\nu = -1$ with large electric field. Because the transverse spin current arises from the Berry curvature of the moiré bands, this broad range demonstrates that the Berry curvature remains substantial far from the $\nu = -1$ band edge. Our observations are consistent with theoretical work predicting uniform Berry curvature [23,27] as well as with the nearly uniform Berry curvature condition needed for the observed fractional Chern insulator (FCI) states in the system [30].

C. Current-controlled helical light emission

Having established efficient current control of spin-valley polarization, we now turn to a second key behavior in moiré MoTe_2 : spin-valley polarization-dependent emission helicity. Although magnetism-related phenomena have been observed in several moiré TMD systems, the spontaneous helical light emission is unique to tMoTe_2 because its bilayer form remains a direct band-gap semiconductor, while other TMD moiré systems become an indirect band gap. Details of the emission mechanism have been discussed in depth in previous works [4,10]. In brief, spin-valley-polarized carriers bind to electron-hole pairs in the opposite valley to form singlet trions, which emit in the $\sigma^+(\sigma^-)$ channel for the electron-hole recombination in the $+K(-K)$ valley. In the FM phase, due to spontaneous spin-valley polarization of the doped holes, light emission occurs only in a single valley, leading to circularly

polarized emission at $\mu_0 H = 0$. This circularly polarized emission is observed across the entire sample and disappears above the Curie temperature T_C (Supplemental Material Fig. S5 [24]). As shown below, current control of spin-valley polarization would also allow us to control trion emission helicity.

Figures 3(a) and 3(b) present the spatial maps of circular-polarization-resolved trion photoluminescence. The degree of circular polarization is defined as $\rho = \{[PL(\sigma^-) - PL(\sigma^+)]/[PL(\sigma^-) + PL(\sigma^+)]\}$. The data are taken with linearly polarized excitation at 632.8 nm, with $v = -0.77$ and $I = \pm 35$ nA, matching the experimental conditions of Figs. 2(c) and 2(d). In these spatial maps, domains with opposite signs of ρ on either side of the current channel appear, which switch with the reversal of I . This behavior demonstrates that the switching of the light helicity is caused by the reversal of spin-valley polarization by current, as demonstrated in our RMCD measurements in Fig. 2. Selecting a spot on one of these domains [black dot in Fig. 3(b)], we plot polarization-resolved PL spectra [Figs. 3(c) and 3(d)] for $I = \pm 35$ nA at $\mu_0 H = 0$. The data clearly show that as we reverse the current flow direction, the trion luminescence switches helicity with near-unity polarization. This establishes current control of light-emission helicity. In addition, comparing the polarization-resolved PL spatial maps between magnetization initialized up [Figs. 3(a) and 3(b)] and down [Figs. 3(e) and 3(f)], we observe the same domain behavior as for the RMCD maps in Fig. 2, as expected from the spin-valley Hall torque mechanism.

We next consider the emission helicity as a function of both the applied magnetic field and current. As seen in Fig. 4(a), ρ vs $\mu_0 H$ swept down and up at $I = 0$ and $v = -0.77$ shows hysteretic behavior and finite ρ at zero magnetic field. This is expected for a ferromagnetic system where near-unity ρ arises from spin-valley polarization. The same measurement with injected current [Figs. 4(b) and 4(c)] shows that while hysteresis vs $\mu_0 H$ is still visible, the center of hysteresis moves away from $\mu_0 H = 0$, depending on the current direction. A full dependence of ρ vs both I and $\mu_0 H$ is shown in Fig. 4(d). We observe that the ρ can be continuously tuned as a function of both parameters. ρ vs I and $\mu_0 H$ for both magnetic field sweep directions is shown in Supplemental Material Fig. S6 [24]. The tuning of the trion PL emission helicity as a function of the current is highlighted in Fig. 4(e); it can be continuously varied between σ^+ and σ^- at zero magnetic field. While we do not observe hysteresis in the ρ vs I measurements in the AHM regime, hysteresis in spin-valley polarization vs I is observed at $v = -1$ and finite D/ϵ_0 (Supplemental Material Fig. S7 [24]). This discrepancy is likely due to stronger domain-wall pinning in gapped phases, leading to nonvolatile domains.

Our experimental results can be compared to quantitative calculations using the spin-diffusion equations in a

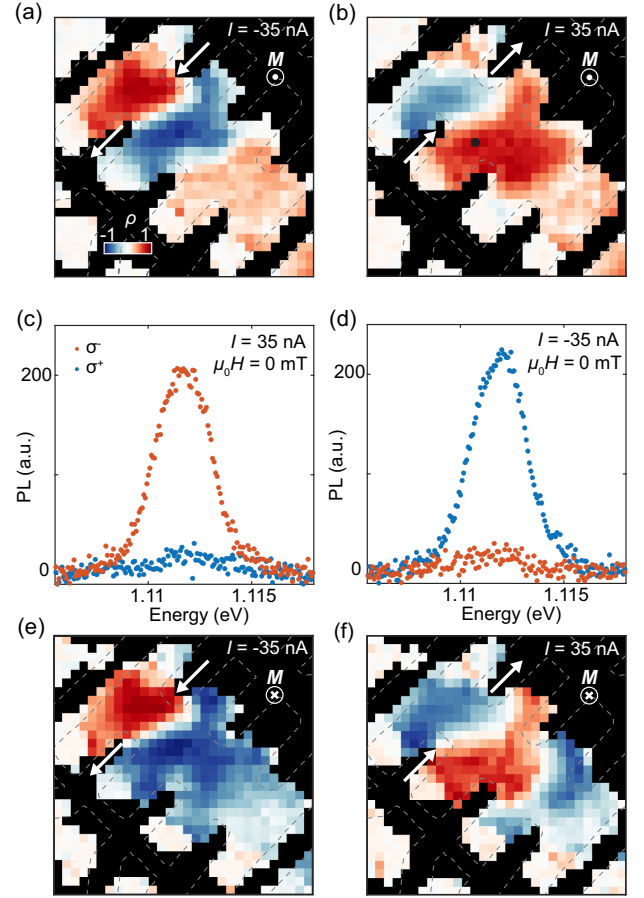


FIG. 3. Current control of helical light emission. (a) Spatial map of PL degree of circular polarization ρ with magnetization initialized to point up. Measurement taken with $I = -35$ nA current and in the anomalous Hall metal regime ($\nu = -0.77$) at $\mu_0 H = 0$ T. Domains with opposite signs of ρ are visible on either side of the current channel. Finite, but smaller, ρ is visible far from the current channel, on the lower-right side of the device. (b) Same as (a), but with $I = 35$ nA. The domain signs are reversed compared to (a). (c) Circular-polarization-resolved PL spectra from the position marked by the black dot in (b). The PL shows clear helicity dependence of the light emission at $\mu_0 H = 0$ T, with the signal predominantly in the σ^- channel. (d) Same as (c), but with $I = -35$ nA, extracted from the same position in (a). The helicity dependence of the PL is switched, with signal now mainly in the σ^+ channel. (e) As in (a), but with magnetization initialized to point down. While the opposite sign of ρ is visible far from the current channel on the lower right of the device, the sign of the domains on either side of the current channel remains the same as in (a), with the same current flow direction but opposite magnetization. (f) As in (b), but with magnetization pointing down. Behavior of domains with switching of current and magnetization direction is consistent with RMCD behavior in Fig. 2.

slab geometry [Fig. 4(f)] [26,31]. We define δM_z as current-induced magnetization and $M_z^0 = g\mu_B n$ as sample magnetization. Here, g is the g factor of charge carriers, μ_B is the Bohr magneton, and n is the carrier density. Using

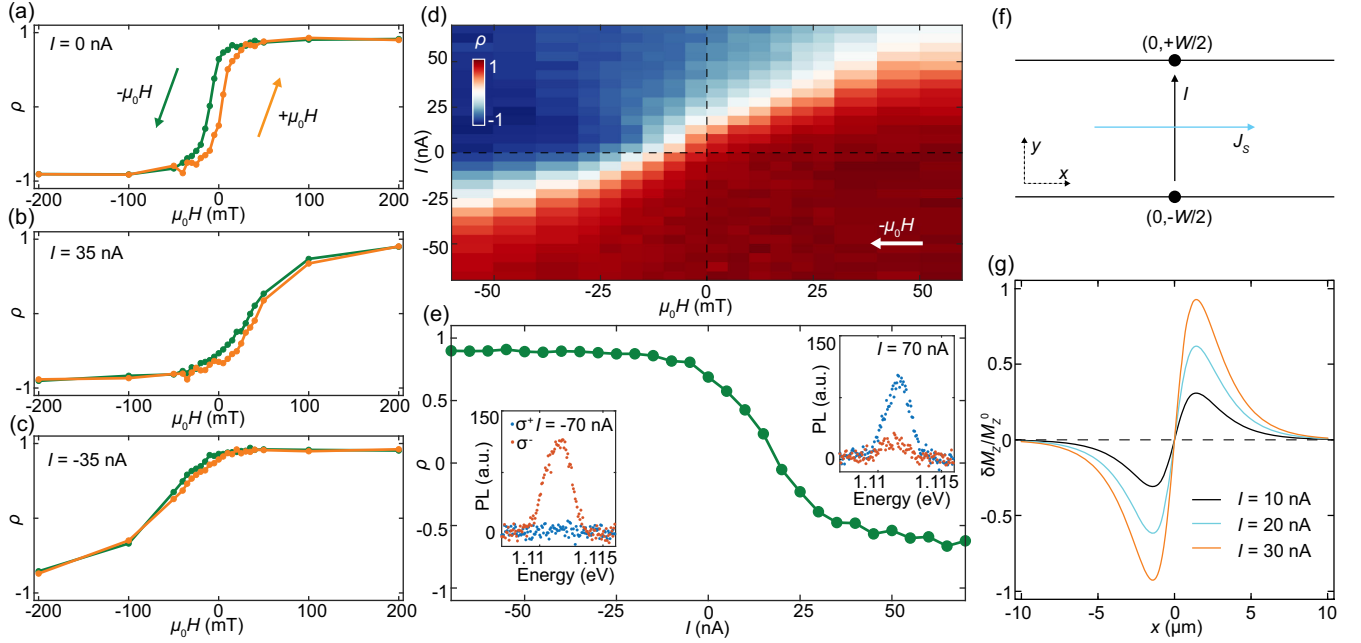


FIG. 4. Continuous tuning of emission helicity via current. (a) ρ vs $\mu_0 H$ swept down and up, with $I = 0$ nA. Hysteresis is visible, indicating that light-emission helicity is controlled by the spin-valley polarization. (b),(c) Same as (a), but with $I = 35$ nA (b) and $I = -35$ nA (c). While hysteresis of ρ vs $\mu_0 H$ is still visible, applied current favors opposite spin-valley polarizations for opposite flow directions. (d) ρ vs I swept down, as a function of $\mu_0 H$, starting from positive $\mu_0 H$. Emission helicity can be continuously tuned between the σ^+ and σ^- channels by both current and magnetic field. (e) ρ as a continuous function of I , at $\mu_0 H = 0$ T, initialized with $\mu_0 H > 0$ T. Insets: helicity-resolved PL emission for large positive and negative current. Helicity can be continuously tuned between these two limits by changing I . All data are taken in the anomalous Hall metal regime, with $\nu = -0.77$, and with the beam spot on the opposite side of the current channel as for Figs. 3(c) and 3(d) (see Supplemental Material Fig. S8 [24]). (f) Schematic of sample current flow configuration, with I and J_s injected charge and transverse spin currents, respectively. Current source and drain are at the black dots, with the current channel length W . (g) Induced magnetization $\delta M_z / M_z^0$ versus x , derived from the spin-diffusion equations and realistic sample parameters at $y = 0$. The critical charge current I_C for magnetization flipping is about 30 nA, the same order of magnitude as experimental observations (see Sec. IV).

realistic sample parameters (see Sec. IV), Fig. 4(g) plots the calculated spatial distribution of $\delta M_z / M_z^0$ for selected charge currents. The calculations show that δM_z has opposite sign at opposite sides of the current channel, and becomes comparable to M_z^0 for a charge current of approximately 30 nA [Fig. 4(g)]. This estimate is on the same order of magnitude as our experimental observation of current switching. A comparison between RMCD data and the modeled spin-diffusion behavior (Supplemental Material Fig. S9 [24]) shows remarkably similar profile, lending additional experimental support for the spin-diffusion picture.

III. CONCLUSIONS

Using RMCD and polarization-resolved PL, we have established current control of spin-valley polarization and helical light emission in moiré MoTe₂. Although the device requires cryogenic temperatures, the strong coupling between electronic, spintronic, and photonic degrees of freedom demonstrated by these results could be appealing in a range of device applications. A particular advantage of

moiré MoTe₂ over other topological or optospintronic systems such as magnetically doped topological insulators or spin light-emitting diodes is that tMoTe₂ is intrinsically topological, ferromagnetic, semiconducting, and optically active, with substantial potential for applications. One possibility is to use these properties to couple magnetic information storage to optical communication within a single device. In addition, the topological phases which occur in tMoTe₂ could open new frontiers in topological optospintronics. As the integer and fractional Chern insulators recently observed in this system have a topological index which depends on the magnetization orientation, the observed spin-valley Hall torque implies that current injection can be used to manipulate these topological states. One interesting direction could be to use current injection to establish two magnetic domains with opposite orientations and investigate the physics arising at the interface between two zero-field FCIs with opposite topological indices. We foresee that establishing current control of magnetic order in moiré MoTe₂ will add an important tuning knob to our toolbox as investigation of these zero-field FCIs and their anyonic excitations continues.

IV. METHODS

A. Device fabrication

The moiré MoTe₂ samples equipped with electrical contacts used in this study were fabricated using the procedure discussed in more depth in Ref. [6]. In brief, van der Waals flakes used in the heterostructure devices—graphite, *h*-BN, and MoTe₂—were mechanically exfoliated on oxygen-plasma-cleaned Si/SiO₂ substrates and identified using an optical microscope. Atomic force microscopy was used to check *h*-BN thickness. A graphite and *h*-BN bottom gate with Pt contacts was prepared using conventional dry-transfer, electron-beam lithography, *e*-beam evaporation, and contact-mode atomic force microscope (AFM) cleaning techniques. In a glovebox with < 0.1 ppm H₂O and O₂ concentrations, monolayer MoTe₂ was exfoliated, and an *h*-BN-encapsulated moiré bilayer was created with the cut-and-stack dry-transfer technique, before putting down on the prepared back gate. After washoff and AFM cleaning of the device, a set of Pt contact gates and Au wire bonding pads were deposited using *e*-beam lithography and evaporation. Finally, the device was AFM cleaned again, before transferring on a top graphite gate.

B. Transport measurements

Transport measurements were taken in a Bluefors dilution refrigerator with a 9-T magnet and base electron temperature of about 80 mK. An ac current bias of 0.2–0.5 nA was generated using a 100-MΩ resistor in series with an ac voltage source (SR830), with the current monitored using a DL1211 current amplifier. Four-terminal R_{xx} and R_{xy} signals were amplified using the differential mode of an SR560 voltage preamplifier with an input resistance (about 100 MΩ) much larger than the contact resistance of the device. The amplified voltage signals were demodulated and measured using SR830 and SR860 lock-ins.

C. Optical measurements

Optical measurements were taken in a closed-loop magneto-optical cryostat (attoDRY 2100) with an attocube xyz piezostage and xy scanners, 9-T z-axis superconducting magnet, and with a base temperature of 1.6 K. Current was applied to the sample using a 100-MΩ resistor in series with a dc voltage source (Keithley 2450) connected to the source pin, with the drain pin grounded. Contact gates were set to −3 V to ensure transparent electrical contact to the moiré MoTe₂, as discussed in Ref. [6]. Polarization-resolved photoluminescence measurements were taken with linearly polarized 632.8-nm HeNe laser excitation focused on the sample by a high-NA nonmagnetic

cryogenic objective to an approximately 1-μm beam spot. Sample emission was collected by the same objective and passed through a quarter wave plate and linear polarizer to select the right- and left-circularly-polarized channels. Signal was then passed through a 75-μm pinhole and dispersed with a diffraction grating (Princeton Instruments, 600 grooves/mm at 1-μm blaze) and detected by a liquid-nitrogen-cooled infrared CCD (Princeton Instruments PyLoN-IR 1.7).

RMCD measurements were taken with excitation near the trion resonance by filtering a broadband supercontinuum source (NKT SuperK Fianium FIR-20) by dual passing through a monochromator to achieve a narrow excitation bandwidth. The out-of-plane magnetization of the sample induces an MCD signal ΔR , the difference between the reflected right- and left-circularly-polarized light. To obtain the normalized RMCD $\Delta R/R$, the laser intensity was chopped at $p = 850$ Hz, and the phase was modulated by $\lambda/4$ via a photoelastic modulator at $f = 50$ kHz. An InGaAs avalanche photodiode detector was used to collect the reflected signal, and the output was read by two lock-in amplifiers (SR830). The ratio between the p -component signal I_p and f -component signal I_f gives the RMCD signal: $\Delta R/R = I_f/[J_1(\pi/2) \times I_p]$ where J_1 is the first-order Bessel function.

D. Determination of doping density and electric field

A parallel plate capacitor model was used to determine the carrier density n and electric field D from the applied top and bottom gate voltages V_{TG} and V_{BG} . Gate capacitances C_{TG} and C_{BG} are calculated using the *h*-BN thickness determined by atomic force microscopy, taking the *h*-BN dielectric constant to be 3.0. Thus, n and D can be computed as $n = (V_{TG}C_{TG} + V_{BG}C_{BG})/e - n_{\text{offset}}$ and $D/\epsilon_0 = (V_{TG}C_{TG} - V_{BG}C_{BG})/2\epsilon_0 - D_{\text{offset}}$, with e the electron charge and ϵ_0 the vacuum permittivity. Carrier density offset n_{offset} is derived from fitting to the insulating states in the PL spectra and transport measurements. D_{offset} is determined from the symmetry axis of the RMCD phase diagram.

E. Induced magnetization and spin Hall current

The magnetization induced by the spin Hall currents can be derived from the spin-diffusion equations [26,31]. The configuration considered is shown in Fig. 4(f). A charge current I is injected in the y direction into a slab of width W , generating a spin current J_S in the x direction to flip the magnetization. Solving the diffusion equation in the slab, the induced magnetization [26,31] is

$$\delta M_z(x, y) = \frac{2g\mu_B I \tan \theta_{SH}}{e l_S^2 / \tau_S} \int \frac{dk}{2\pi} e^{ikx} \frac{\cosh(\omega_k y)}{\omega_k \coth(kW/2) \sinh(\omega_k W/2) + 4k \tan^2(\theta_{SH}) \cosh(\omega_k W/2)},$$

where g is the g factor of charge carriers, μ_B is the Bohr magneton, θ_{SH} is the spin Hall angle, e is the electron charge. l_S is the spin-diffusion length, and τ_s is the spin relaxation time $\omega_k = \sqrt{k^2 + l_S^{-2}}$.

The calculation parameters are estimated from experimental values. $W = 3 \mu\text{m}$ is the distance between electrical contacts. To estimate the value of l_S , we note that experimentally the size of the flipped domain is on the order of μm , indicating l_S should be on the same order. We choose $l_S = 1 \mu\text{m}$. The spin Hall angle is defined by $\tan \theta_{\text{SH}} = e\sigma_{\text{SH}}/\hbar\sigma_{xx}$, where σ_{SH} is the spin Hall conductivity, σ_{xx} is the longitudinal conductivity, and \hbar is the reduced Planck constant. $\sigma_{\text{SH}} = (\sigma_{H,K} - \sigma_{H,K'})\hbar/2e$ (Ref. [32]) due to spin-valley coupling in TMDs, with $\sigma_{H,K}$ and $\sigma_{H,K'}$ the Hall conductivities of valleys K and K' . If we assume the system is fully polarized to K , σ_{SH} is simply $\sigma_{H,K}\hbar/2e = \hbar\sigma_{\text{AH}}/2e$, and σ_{AH} is the anomalous Hall conductivity. Thus, $\tan \theta_{\text{SH}} = \sigma_{\text{AH}}/2\sigma_{xx}$. The experimentally measured longitudinal resistance ρ_{xx} and anomalous Hall resistance ρ_{xy} are both on the same order of a few $\text{k}\Omega$. We thus take $\tan \theta_{\text{SH}} = \sigma_{\text{AH}}/2\sigma_{xx} = \rho_{xy}/2\rho_{xx} = 1/2$. Finally, while τ_s cannot be determined directly from our measurement, τ_s in TMD heterobilayers is estimated to be on the order of μs in Refs. [26,33]. We take τ_s to be on the same order here, $\tau_s = 5 \mu\text{s}$.

Figure 4(g) shows the induced magnetization δM_z vs position x at the center of the slab ($y = 0$) for different injection currents I . The magnetization flipping occurs when the peak of δM_z is on the order of M_z^0 , where M_z^0 is the magnetization of the ground state. $M_z^0 = g\mu_B n$, and carrier density $n = -3.8 \times 10^{12} \text{ cm}^{-2}$ for the filling $\nu = -0.78$ in our experimental sample. With our choice of τ_s , the critical current for magnetization flipping is on the order of 30 nA, consistent with the experimental values.

ACKNOWLEDGMENTS

This project is mainly supported by the U.S. Department of Energy, Office of Science, Basic Energy Sciences, under Award No. DE-SC0018171. The electrical control of ferromagnetism is partially supported by Vannevar Bush Faculty Fellowship (Award No. N000142512047), and theory is supported by Grant No. DE-SC0012509. E. A. acknowledges support by the National Science Foundation Graduate Research Fellowship Program under Grant No. DGE-2140004. The authors also acknowledge the use of the facilities and instrumentation supported by NSF Grant No. MRSEC DMR-1719797. K. W. and T. T. acknowledge support from the JSPS KAKENHI (Grants No. 21H05233 and No. 23H02052), the CREST (Grant No. JPMJCR24A5), JST and World Premier International Research Center Initiative, MEXT, Japan. X. X. acknowledges support from the State of Washington funded Clean Energy Institute and from the Boeing Distinguished Professorship in Physics.

X. X. conceived and supervised the experiment. H. P. fabricated and performed the transport measurements, assisted by J. C. E. A. performed the magneto-optical measurements. E. A., X. X., D. X., T. C., and L. F. analyzed and interpreted the results. K. Y. and D. X. performed the calculations. T. T. and K. W. synthesized the h -BN crystals. E. A., X. X., and D. X. wrote the paper with input from all authors. All authors discussed the results.

The authors declare no competing interests.

DATA AVAILABILITY

The data that support the findings of this article are openly available [34].

-
- [1] Y. Cao, V. Fatemi, S. Fang, K. Watanabe, T. Taniguchi, E. Kaxiras, and P. Jarillo-Herrero, *Unconventional superconductivity in magic-angle graphene superlattices*, *Nature (London)* **556**, 7699 (2018).
 - [2] R. Bistritzer and A. H. MacDonald, *Moiré bands in twisted double-layer graphene*, *Proc. Natl. Acad. Sci. U.S.A.* **108**, 12233 (2011).
 - [3] F. Wu, T. Lovorn, E. Tutuc, I. Martin, and A. H. MacDonald, *Topological insulators in twisted transition metal dichalcogenide homobilayers*, *Phys. Rev. Lett.* **122**, 086402 (2019).
 - [4] J. Cai *et al.*, *Signatures of fractional quantum anomalous Hall states in twisted MoTe₂*, *Nature (London)* **622**, 7981 (2023).
 - [5] Y. Zeng, Z. Xia, K. Kang, J. Zhu, P. Knüppel, C. Vaswani, K. Watanabe, T. Taniguchi, K. F. Mak, and J. Shan, *Thermodynamic evidence of fractional Chern insulator in moiré MoTe₂*, *Nature (London)* **622**, 7981 (2023).
 - [6] H. Park *et al.*, *Observation of fractionally quantized anomalous Hall effect*, *Nature (London)* **622**, 7981 (2023).
 - [7] F. Xu *et al.*, *Observation of integer and fractional quantum anomalous Hall effects in twisted bilayer MoTe₂*, *Phys. Rev. X* **13**, 031037 (2023).
 - [8] E. Redekop *et al.*, *Direct magnetic imaging of fractional Chern insulators in twisted MoTe₂*, *Nature (London)* **635**, 584 (2024).
 - [9] Z. Ji, H. Park, M. E. Barber, C. Hu, K. Watanabe, T. Taniguchi, J.-H. Chu, X. Xu, and Z.-X. Shen, *Local probe of bulk and edge states in a fractional Chern insulator*, *Nature (London)* **635**, 578 (2024).
 - [10] E. Anderson *et al.*, *Trion sensing of a zero-field composite Fermi liquid*, *Nature (London)* **635**, 590 (2024).
 - [11] Z. Lu, T. Han, Y. Yao, A. P. Reddy, J. Yang, J. Seo, K. Watanabe, T. Taniguchi, L. Fu, and L. Ju, *Fractional quantum anomalous Hall effect in multilayer graphene*, *Nature (London)* **626**, 759 (2024).
 - [12] T. Neupert, L. Santos, C. Chamon, and C. Mudry, *Fractional quantum Hall states at zero magnetic field*, *Phys. Rev. Lett.* **106**, 236804 (2011).
 - [13] N. Regnault and B. A. Bernevig, *Fractional Chern insulator*, *Phys. Rev. X* **1**, 021014 (2011).

- [14] D. N. Sheng, Z.-C. Gu, K. Sun, and L. Sheng, *Fractional quantum Hall effect in the absence of Landau levels*, *Nat. Commun.* **2**, 1 (2011).
- [15] K. Sun, Z. Gu, H. Katsura, and S. Das Sarma, *Nearly flatbands with nontrivial topology*, *Phys. Rev. Lett.* **106**, 236803 (2011).
- [16] E. Tang, J.-W. Mei, and X.-G. Wen, *High-temperature fractional quantum Hall states*, *Phys. Rev. Lett.* **106**, 236802 (2011).
- [17] D. Xiao, W. Zhu, Y. Ran, N. Nagaosa, and S. Okamoto, *Interface engineering of quantum Hall effects in digital transition metal oxide heterostructures*, *Nat. Commun.* **2**, 1 (2011).
- [18] B. A. Bernevig and N. Regnault, *Emergent many-body translational symmetries of Abelian and non-Abelian fractionally filled topological insulators*, *Phys. Rev. B* **85**, 075128 (2012).
- [19] C. Ruppert, B. Aslan, and T. F. Heinz, *Optical properties and band gap of single- and few-layer MoTe₂ crystals*, *Nano Lett.* **14**, 6231 (2014).
- [20] I. G. Lezama, A. Arora, A. Ubaldini, C. Barreteau, E. Giannini, M. Potemski, and A. F. Morpurgo, *Indirect-to-direct band gap crossover in few-layer MoTe₂*, *Nano Lett.* **15**, 2336 (2015).
- [21] E. Anderson, F.-R. Fan, J. Cai, W. Holtzmann, T. Taniguchi, K. Watanabe, D. Xiao, W. Yao, and X. Xu, *Programming correlated magnetic states with gate-controlled moiré geometry*, *Science* **381**, 325 (2023).
- [22] P. A. Dainone *et al.*, *Controlling the helicity of light by electrical magnetization switching*, *Nature (London)* **627**, 783 (2024).
- [23] V. Crépel and L. Fu, *Anomalous Hall metal and fractional Chern insulator in twisted transition metal dichalcogenides*, *Phys. Rev. B* **107**, L201109 (2023).
- [24] See Supplemental Material at <http://link.aps.org/supplemental/10.1103/ds5p-763x> for additional RMCD measurements versus v and D/ϵ_0 , RMCD spatial maps with alternate pin configurations and selected currents, emission helicity above T_C , current sweep hysteresis measurements, and a comparison between modeled spin-diffusion and experimental data.
- [25] C. L. Tschirhart *et al.*, *Intrinsic spin Hall torque in a moiré Chern magnet*, *Nat. Phys.* **19**, 807 (2023).
- [26] Z. Tao *et al.*, *Giant spin Hall effect in AB-stacked MoTe₂/WSe₂ bilayers*, *Nat. Nanotechnol.* **19**, 28 (2024).
- [27] T. Devakul, V. Crépel, Y. Zhang, and L. Fu, *Magic in twisted transition metal dichalcogenide bilayers*, *Nat. Commun.* **12**, 6730 (2021).
- [28] T. Devakul and L. Fu, *Quantum anomalous Hall effect from inverted charge transfer gap*, *Phys. Rev. X* **12**, 021031 (2022).
- [29] T. Li *et al.*, *Quantum anomalous Hall effect from intertwined moiré bands*, *Nature (London)* **600**, 7890 (2021).
- [30] C. Wang, X.-W. Zhang, X. Liu, Y. He, X. Xu, Y. Ran, T. Cao, and D. Xiao, *Fractional Chern insulator in twisted bilayer MoTe₂*, *Phys. Rev. Lett.* **132**, 036501(R) (2024).
- [31] M. Beconcini, F. Taddei, and M. Polini, *Nonlocal topological valley transport at large valley Hall angles*, *Phys. Rev. B* **94**, 121408 (2016).
- [32] J. Sinova, S. O. Valenzuela, J. Wunderlich, C. H. Back, and T. Jungwirth, *Spin Hall effects*, *Rev. Mod. Phys.* **87**, 1213 (2015).
- [33] E. C. Regan *et al.*, *Mott and generalized Wigner crystal states in WSe₂/WS₂ moiré superlattices*, *Nature (London)* **579**, 359 (2020).
- [34] E. Anderson, H. Park, K. Yang, J. Cai, T. Taniguchi, K. Watanabe, L. Fu, T. Cao, and X. Xu, Dataset for: Magnetoelectric Control of Helical Light Emission in a Moiré Chern Magnet (2025) [Data set]. Zenodo, 10.5281/zenodo.16883546.